Applied Catalysis B: Environmental 238 (2018) 27–37

Contents lists available at ScienceDirect

Applied Catalysis B: Environmental

journal homepage: www.elsevier.com/locate/apcatb

Stable multiphasic 1T/2H $MoSe_2$ nanosheets integrated with 1D sulfide semiconductor for drastically enhanced visible-light photocatalytic hydrogen evolution

Nan Li[a], Jiaojiao Wu[a], Yanting Lu[a], Zhijie Zhao[a], Hechuan Zhang[a], Xitao Li[a], Yan-Zhen Zheng[b,**], Xia Tao[a,b,*]

[a] State Key Laboratory of Organic-Inorganic Composites, Beijing University of Chemical Technology, Beijing 100029, China
[b] Research Center of the Ministry of Education for High Gravity Engineering & Technology, Beijing University of Chemical Technology, Beijing 100029, China

ARTICLE INFO

Keywords:
Cocatalyst
1T/2H $MoSe_2$
CdS
Visible light
H_2 evolution

ABSTRACT

Low-cost and efficient noble-metal-free cocatalysts on semiconductors are highly desirable for visible-light photocatalytic hydrogen evolution reaction (HER). Herein, we report the synthesis and characterizations of novel and high-efficiency noble-metal-free multiphasic $MoSe_2$ nanosheets composed of metallic 1T phase and semiconducting 2H phase $MoSe_2$ (denoted as 1T/2H $MoSe_2$), and their implementation as cocatalysts to form photocatalytic heterostructure with 1D CdS nanorods (denoted as 1T/2H-MC). For comparison, conventional 2H $MoSe_2$ and corresponding heterostructure 2H $MoSe_2$/CdS i.e. 2H-MC were synthesized in parallel. The spectroscopic/electrochemical assays show that the 1 T/2H $MoSe_2$ cocatalyst exhibits narrower bandgap, more active sites and better conductivity with respect to 2H $MoSe_2$. As a consequence, the optimized 1T/2H-MC-10% exhibits drastically enhanced visible-light (λ > 420 nm) photocatalytic HER rate of 93.4 mmol/g/h, obviously higher than those of bare CdS (10.8 mmol/g/h), 2H-MC-10% (30.4 mmol/g/h) and Pt/CdS (50.4 mmol/g/h), respectively. Such an H_2 production rate also exceeds all reported $MoSe_2$-based heterostructure photocatalysts. Most importantly, the multiphasic 1 T/2H $MoSe_2$ remained stable after aging for several months and the HER activity of the 1 T/2H-MC-10% was demonstrated to have no decay even after 8 cycling of visible-light HER.

1. Introduction

Hydrogen (H_2) is viewed as an ideal energy carrier, due to its advantages of environmental friendliness with H_2O being the unique oxidation product, good compatibility with other state-of-the-art energy technologies, together with high energy capacity of 143 MJ/kg [1,2]. Over recent years, H_2 evolution via photocatalytic water splitting has achieved significant interest and emerged with potential as the primary method. In conventional photocatalytic systems, cocatalysts not only assist the electron-hole separation at the cocatalyst/semiconductor interface, but also supply active sites for H_2 evolution [3]. Though noble-metal-based cocatalysts, such as Pd, Pt, and Au, have been widely used as efficient cocatalysts for photocatalytic hydrogen evolution reaction (HER) [4–7], exploration of alternative low-cost and high-activity cocatalysts in place of noble metals still is a research hotspot [8–12].

In the past few decades, transition metal dichalcogenide compounds with a general formula MX_2 (M = Mo or W, X=S or Se) have been found to display high activity for the electrocatalytic/photocatalytic HER process [13–17]. Particularly, MoS_2 has been widely investigated as a non-noble-metal cocatalyst for the modification of semiconductor photocatalysts toward sustainable H_2 evolution [18,19]. Compared to more extensively studied MoS_2, $MoSe_2$ possesses intriguing characteristics such as lower Gibbs free energy ($\Delta G_H \sim 0.05$ eV, close to thermoneutral) and higher electrical conductivity originated from its intrinsic metallic nature capable of being a compelling cocatalyst candidate for photocatalytic HER [20,21]. To the best of our knowledge, only a few recent reports focus on $MoSe_2$ cocatalyst for photocatalytic HER [22–24]. For instance, Liu's group designed a $MoSe_2$/TiO_2 heterostructure photocatalyst with a maximum photocatalytic H_2 evolution rate of 0.4682 mmol/g/h [22]. Yang and co-workers reported that the photocatalytic HER activities of $ZnIn_2S_4$ can be improved by loading an amount of $MoSe_2$, with an optimized visible-light-driven HER rate of 6.454 mmol/g/h [23]. Apparently, the HER activities of $MoSe_2$-based photocatalysts in the existing reports are far

* Corresponding author at: State Key Laboratory of Organic-Inorganic Composites, Beijing University of Chemical Technology, Beijing 100029, China.
** Corresponding author.
E-mail addresses: taoxia@mail.buct.edu.cn, taoxia@yahoo.com (X. Tao).

https://doi.org/10.1016/j.apcatb.2018.07.002
Received 9 May 2018; Received in revised form 26 June 2018; Accepted 1 July 2018
Available online 03 July 2018
0926-3373/

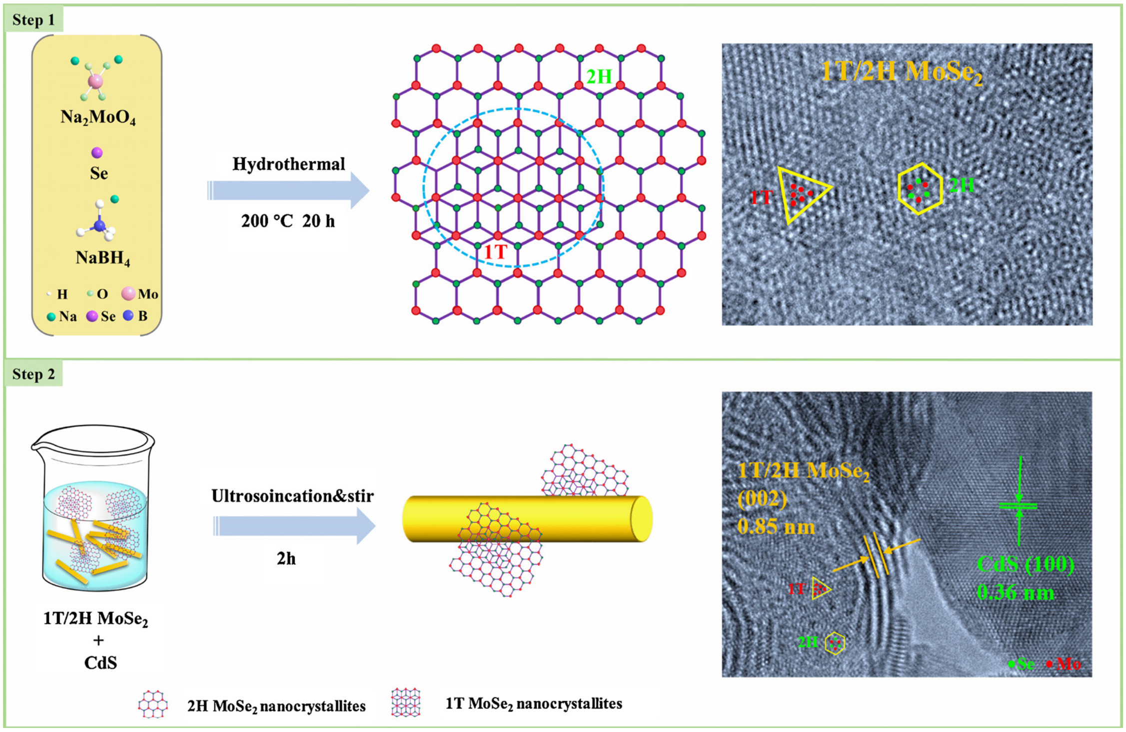

Scheme 1. Synthetic route for the 1T/2H $MoSe_2$ cocatalyst and 1 T/2H-MC heterostructure photocatalyst.

unsatisfactory.

In fact, $MoSe_2$ has two phases according to the arrangement of Se atoms: semiconducting 2H phase with trigonal prismatic and metastable metallic 1 T phase with octahedral coordination [25]. Although original 2H phase $MoSe_2$ appears to have good intrinsic HER activity in proven photocatalytic systems, 1 T phase $MoSe_2$ possesses more favorable properties such as proliferated active sites and metallic electronic conductivity [26]. It has been demonstrated that pure 1 T phase or miscellaneous 1 T/2H phase $MoSe_2$ can boost the intrinsic activity of catalysts in electrocatalytic HER and lithium ionic anode systems [25–28]. However, the usual preparation procedures associated with pure 1 T phase $MoSe_2$ are tedious, accompanied by high risk of using metallic lithium. Again, the obtained 1 T phase $MoSe_2$ is thermodynamically metastable, which tends to form stable 2H phase $MoSe_2$ by restacking [29]. Thus, in this context, we attempt to construct a stable multiphasic 1 T/2H $MoSe_2$ cocatalyst, combining abundant active sites and good conductivity of 1 T phase with environmental stability of 2H phase, and then integrate with a semiconductor to achieve high-performance HER photocatalyst, which has yet to be reported so far.

In this study, we report the synthesis of novel and high-efficiency multiphasic 1 T/2H $MoSe_2$ nanosheets via a facile hydrothermal method, and their implementation as cocatalysts for photocatalytic HER over 1D CdS nanorods. We demonstrate that the stable multiphasic structure of 1 T/2H $MoSe_2$ can not only provide abundant reactive sites beneficial to H_2 evolution, but also increase photogenerated charge transfer and consequently reduce carrier recombination probability. As a result, it is found that the as-obtained 1 T/2H-MC photocatalysts exhibit better HER activities than 2H-MC. Particularly, the optimized 1 T/2H-MC-10% exhibits the highest visible-light (λ > 420 nm) photocatalytic HER rate up to 93.4 mmol/g/h, obviously higher than those of pure CdS (10.8 mmol/g/h), 2H-MC-10% (30.4 mmol/g/h) and even Pt/CdS (50.4 mmol/g/h). Considering its low-cost, abundant active sites, good electronic conductivity and stability of 1 T/2H $MoSe_2$, we expected that the 1 T/2H $MoSe_2$-based photocatalyst is a hopeful competitor for high-efficiency photocatalytic H_2 evolution.

2. Experimental section

2.1. Materials synthesis

2.1.1. Preparation of 1 T/2H $MoSe_2$ and 2H $MoSe_2$

Typically, 0.304 g $NaBH_4$, 0.316 g Se and 0.484 g Na_2MoO_4 were mixed together and then dissolved in 75 mL distilled water. In order to obtain a homogeneous solution, a vigorous magnetic stirring was performed for 20 min, and the solution was subsequently transferred into a 100 mL Teflon-lined stainless steel autoclave. The autoclave was heated in a conventional oven to 200 °C and maintained at the target temperature for 20 h. After cooling naturally, the black precipitate was collected by centrifugation, washed with deionized water and absolute ethanol for several times and dried at 60 °C under vacuum. To obtain 2H $MoSe_2$, the as-prepared 1 T/2H $MoSe_2$ sample was annealed at 600 °C at a rate of 10 °C/min and maintained at this temperature for 1 h, then allowed to cool down to room temperature naturally under argon atmosphere.

2.1.2. Preparation of CdS

CdS was synthesized by a solvothermal method [30]. In a typical procedure, 4.624 g $CdCl_2{\cdot}2.5H_2O$ and 4.624 g NH_2CSNH_2 were added into a Teflon-lined stainless steel autoclave filled with ethylenediamine to 80% of its capacity (100 mL). The autoclave was sealed and heated in an oven at 160 °C for 48 h. The resultant precipitates were collected by centrifugation and washed with distilled water and ethanol several times. Finally, the precipitates were dried in vacuum at 60 °C for 12 h.

2.1.3. Preparation of the heterostructure catalysts

The 1 T/2H-MC or 2H-MC powders were synthesized by a simple sonicating and stirring method. The 500 mg CdS powder with 10 wt % 1 T/2H $MoSe_2$ or 2H $MoSe_2$ were added into 30 mL ethanol, followed by sonicating for 1 h and stirring for 1 h to form a homogeneous solution. Subsequently, the ethanol was evaporated at 80 °C to gain the target 1 T/2H-MC-10% or 2H-MC-10% heterostructure catalysts. Other composite photocatalysts with diff ;erent weight percent of 1 T/2H-MC or 2H-MC were similarly prepared and labeled. A schematic

representation of the synthesis procedure is shown in Scheme 1.

2.2. Characterizations

X-ray diffraction (XRD) patterns of products were investigated by X-ray diffraction analysis (X'Pert PRO MPD, Panalytical) using Cu Kα radiation at 40 kV and 40 mA. Morphology of samples were observed by scanning electron microscopy (SEM) images on a Hitachi S-4700 microscope, and its composition was examined using energy dispersive spectroscopy (EDS) attached to the SEM. The Brunauer–Emmett–Teller (BET) specific surface area and the Barrett–Joyner–Halenda (BJH) pore-size distribution were taken using a Quantachorme Quadrasorb SI instrument. High resolution transmission electron microscopy (HRTEM) images of the synthesized products were carried out on a Hitachi H-9500 microscope. The absorption spectra were obtained using UV–vis spectrophotometry (Lambda 950, Perkin Elmer). X-ray photoelectron spectroscopy (XPS) analysis was performed on a Thermo ESCALAB250 X-ray photoelectron spectrometer using Al Ka as an X-ray source. Electron spin resonance (EPR) spectrum was acquired using a JEOL JES-FA200 X-band spectrometer. Zeta-potentials of the samples in water were measured by a Malvern zeta analyzer (Nano-ZS 90, Malvern Instrument, UK). Photoluminescence (PL) emission and time-resolved spectra were obtained on a Spectrofluorometer FS5 (EDINBURGH INSTRUMENTS) with an excitation wavelength of 426 nm at room temperature.

2.3. Photoelectrochemical measurements

Photoelectrochemical measurements were performed in a standard three-electrode quartz cell with a H_2SO_4 (cocatalyst system) or Na_2SO_4 (heterostructure catalyst system) electrolyte solution, an Ag/AgCl electrode was used as the reference electrode. As for cocatalysts, a graphite rod and glassy carbon electrode loaded with various cocatalysts (1T/2H $MoSe_2$ and 2H $MoSe_2$) samples were chosen as the counter electrode and the working electrodes, respectively. As for heterostructure catalysts, a platinum wire and the heterostructure samples (1T/2H-MC or 2H-MC) were used as the counter electrode and the working electrodes, respectively. A typical preparation procedure for the 1T/2H $MoSe_2$ and 2H $MoSe_2$ based working electrodes as follows: 10 mg cocatalyst and 80 μL Nafion were dispersed in 3 mL water-ethanol solution (volume ratio of 3:1), followed by sonicating for 1 h to form a homogeneous solution. Then 10 μL dispersion was dripped onto a glassy carbon electrode with 3 mm diameter. And a typical preparation procedure for the heterostructure materials based working electrodes as follows: 10 mg 1 T/2H-MC or 2H-MC catalysts were dispersed into a ternary solution containing 100 μL Nafion, 400 μL ethanol and 500 μL H_2O by 1 h sonication to prepare a homogeneous colloid. Then, all of the catalyst colloid was deposited on the indiumtin oxide conductive glass with area of 1 cm^2 and then dried in air to form the working electrode. A 300 W metal halide lamp equipped with a 420 nm cutoff filter was adopted as a light source. Mott–Schottky plots were obtained under direct current potential polarization at different frequencies (1000, 3000, 10,000 HZ). Electrochemical impedance spectroscopy (EIS) was recorded at the open-circuit potential, and the frequency range was fixed from 0.01 to 10^5 HZ. The photocurrent density-voltage (I–V) curves were measured in the bias sweep range −1 to 1 V. The electrochemically capacitance measurements were conducted by cyclic voltammograms from -1 to 1 V with various scan rates (10, 20, 40, 60, 80, 100, 120 mV/s).

2.4. Photocatalytic H_2 evolution

The photocatalytic H_2 production experiments were performed in an outer irradiation type photoreactor (50 mL quartz glass). 2 mg photocatalyst was suspended in 20 mL aqueous solution containing 10 vol% of lactic acid solution. Before irradiation, the suspension was thoroughly degassed to remove air by bubbling N_2 for 30 min. During the water splitting experiment, the suspension was stirred and irradiated by a 300 W metal halide lamp equipped with 420 nm cut off filter. The amount of evolved H_2 was analyzed by gas chromatography (Agilent 7890B) with high-purity nitrogen carrier gas. The AQE was measured at 420 nm, 450 nm, 500 nm, 550 nm, 600 nm and 700 nm monochromatic lights which were obtained by using band-pass filters for 1 h. For the AQE at 420 nm, the average intensity of irradiation was determined to be 30 mW/cm^2 and the irradiation area was 1 cm^2 (exposing a window with a length of 1 cm and width of 1 cm). For the AQE at 600 nm, the average intensity of irradiation was measured to be 15 mW/cm^2 and the irradiation area was also 1 cm^2. The AQE was then calculated by the following Eq. (1):

$$\mathrm{AQY}(\%) = \frac{2 \times \text{number of evolved } H_2 \text{ molecules}}{\text{number of incident photons}} \times 100\% \tag{1}$$

3. Results and discussion

3.1. Structure and property of cocatalysts

The 1 T/2H $MoSe_2$ cocatalyst was prepared via a facile hydrothermal method using $NaMoO_4{\cdot}2H_2O$ and Se as precursors, and a certain amount of $NaBH_4$ as reductant (see Scheme 1). The SEM image (Fig. 1a) shows that the as-obtained 1 T/2H $MoSe_2$ is composed of small particles with about 70–90 nm in size. The TEM image (Fig. 1b) gives a clear view of nanoflower structures on 1 T/2H $MoSe_2$, which are assembled from interconnected nanosheets. An inter-planar spacing of the (002) plane about 0.85 nm is observed in the HRTEM image of 1 T/2H $MoSe_2$ nanosheets (Fig. 1c), which is obviously larger than (002) plane of 2H $MoSe_2$ (0.65 nm, JCPDS No.29-0914). Such increased inter-planar spacing is believed to be due to the transition from 2H phase to 1 T phase $MoSe_2$ [31]. Further, both 1 T and 2H phases could simultaneously be visualized in 1 T/2H $MoSe_2$ crystal structure (Fig. 1d). Further zoom-in HRTEM images (Fig. 1e-f) provide the detailed atom arrangements of 1 T and 2H phases in 1 T/2H $MoSe_2$ microstructure. All the above results and analysis verify the coexistence of 2H and 1 T phases in 1 T/2H $MoSe_2$ matrix. From Fig. S1a-b, a nanoflower morphology of 2H $MoSe_2$ similar to that of 1 T/2H $MoSe_2$ and the inter-planar spacing of about 0.65 nm for 2H $MoSe_2$ were also observed. Structural representation of 2H $MoSe_2$ and 1 T/2H $MoSe_2$ and their corresponding metal atoms coordination are shown in Fig. S2.

To further determine the compositions and phase states of as-prepared $MoSe_2$ samples, XRD, Raman and XPS analyses were experimentally conducted. In the XRD patterns (Fig. 2a), the (002) peak of 1 T/2H $MoSe_2$ slight shifts with an angle of ≈ 1.3° and the peak intensity decreases as compared to 2H $MoSe_2$. The above changes in the XRD results are consistent with those reported for the transition from 2H phase to 1 T phase $MoSe_2$ [13,31]. Raman spectra analysis is a powerful method to determine the phases of transition metal dichalcogenide compounds. The spectrum (Fig. 2b) of 2H $MoSe_2$ displays only two prominent peaks corresponding to the in-plane A_{1g} and out-of-plane E^1_{2g} modes [32]. As for 1 T/2H $MoSe_2$, additional strong peaks at 195 (J_1), 350 (J_2), 484 (J_3) cm^{-1} are emerging, implying the existence of 1 T phase in 1 T/2H $MoSe_2$ [27]. Furthermore, the similarity in XRD patterns and Raman spectra between few-months aged and fresh 1 T/2H $MoSe_2$ samples (Fig. S3a-b) strongly confirm the high stability of multiphasic 1 T/2H $MoSe_2$ materials. XPS was employed to investigate the chemical compositions of samples. For 2H $MoSe_2$ sample (Fig. 3a), two characteristic peaks at 229.4 eV (Mo $3d_{5/2}$) and 232.8 eV (Mo $3d_{3/2}$) were detected [25]. As for 1 T/2H $MoSe_2$, the Mo 3d spectra have obvious peak-width change and negative peak-shift. The broadened peaks of Mo $3d_{5/2}$ and Mo $3d_{3/2}$ can further be deconvoluted to two double peaks i.e. 228.6 eV (1 T phase) and 229.4 eV (2H phase), 231.9 eV (1 T phase) and 232.6 eV (2H phase), respectively. These results indicate that 1 T phase coexists with 2H phase in 1 T/2H $MoSe_2$

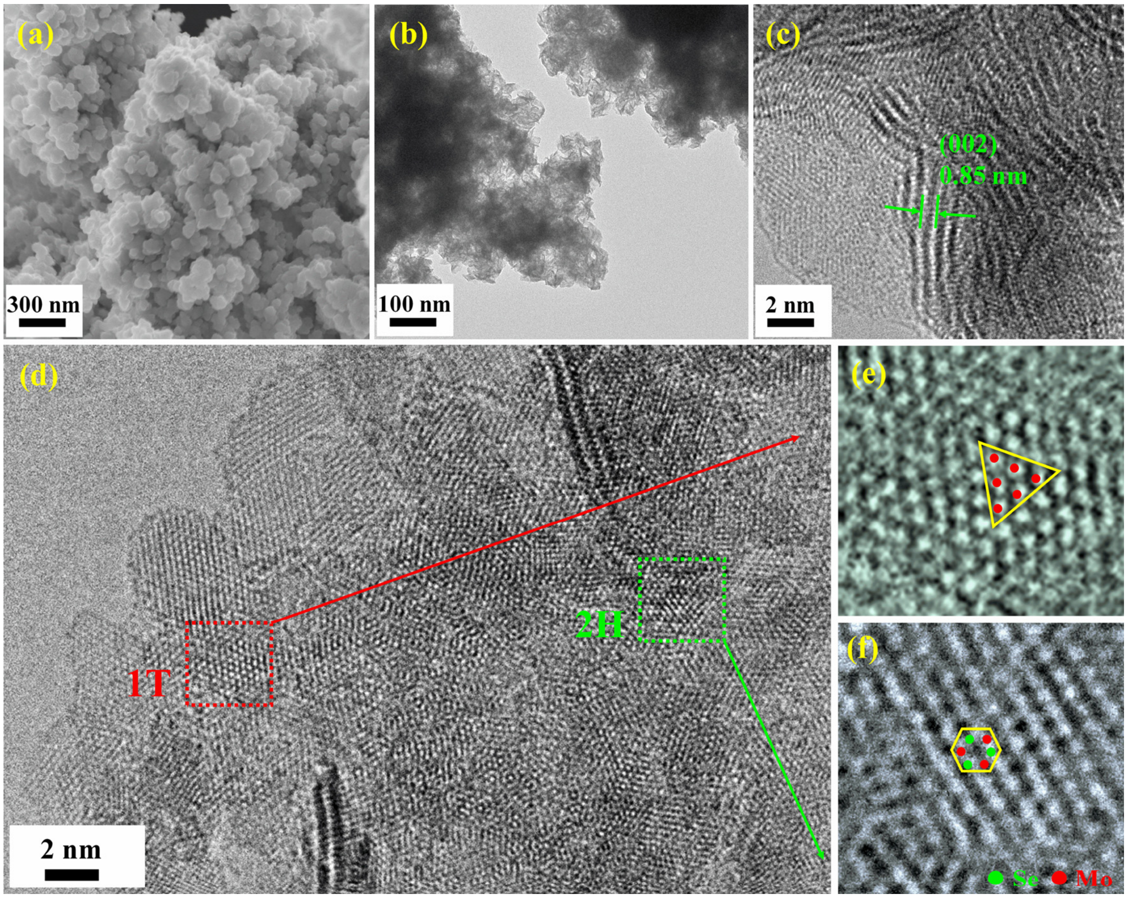

Fig. 1. (a) SEM, (b) TEM, (c–d) HRTEM images of the as-prepared 1 T/2H $MoSe_2$. (e–f) Images of the region enclosed by the square of (d).

[33]. Besides, the XPS spectra of Se (Fig. 3b) also provide more evidences for the coexistence of 1 T and 2H in 1 T/2H $MoSe_2$. Specifically, for 2H $MoSe_2$ sample, Se 3d spectra exhibit two typical peaks at 54.6 and 55.5 eV belonging to the Se^{2-}. In contrast, four deconvoluted peaks at 54.1, 54.6, 54.9 and 55.5 eV appear for 1 T/2H $MoSe_2$ sample, among which the peaks at 54.1 and 54.9 eV are reasonably assigned to the 1 T phase of Se^{2-}. The content of 1 T phase in 1 T/2H $MoSe_2$ is calculated to be ~ 34.5%. All these observations mutually support the successful preparation of 1 T/2H $MoSe_2$.

UV–vis spectra of 2H $MoSe_2$ and 1 T/2H $MoSe_2$ were collected in Fig. 4a. The 1 T/2H $MoSe_2$ shows enhanced light absorption than 2H $MoSe_2$ throughout the whole UV–vis wavelength range. Moreover, the band gap of 2H $MoSe_2$ and 1 T/2H $MoSe_2$ is determined as ~ 1.14 and 0.65 eV by the estimate of straight line to X-axis intercept from the plot of $(\alpha h\nu)^2$ versus $h\nu$ (Fig. 4b) [34]. Additionally, the electrocatalytic activities of 2H $MoSe_2$ and 1 T/2H $MoSe_2$ were characterized by a series of electrochemical assays. The polarization curves show the normalized current density versus voltage for 2H $MoSe_2$ and 1 T/2H $MoSe_2$ as shown in Fig. 4c. 1T/2H $MoSe_2$ displays a lower onset overpotential and a larger cathodic current density than 2H $MoSe_2$, demonstrating the excellent electrocatalytic activity [15]. To compare the intrinsic activities of diff ;erent catalysts, the electrochemical capacitance plots (Fig. S4) were performed to determine the active surface area of the catalysts. According to the method in the literature [35], 1 T/2H $MoSe_2$ shows a calculated electrochemically active surface area value of 30.28 cm^2, significantly larger than that of the 2H $MoSe_2$ (by ~ 7 times), providing more active sites. Obviously, 1 T phase could give rise to enrichment effect of active sites for 1 T/2H $MoSe_2$ beneficial to the photocatalytic HER [36]. EIS was also conducted to provide further insight into the electrode kinetics during HER. From Fig. 4d and Table S1, charge-transfer resistance (R_{ct}) values obtained for 1 T/2H $MoSe_2$ and 2H $MoSe_2$ are 198 Ω and 2920 Ω, respectively. A smaller R_{ct} of 1 T/

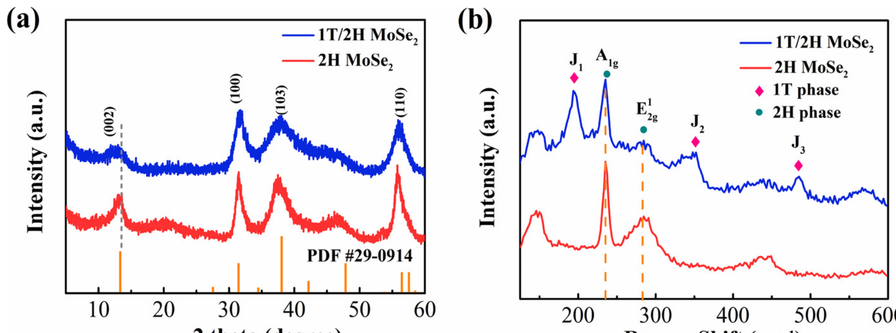

Fig. 2. Characterization of 1T/2H $MoSe_2$ and 2H $MoSe_2$: (a) XRD pattern, (b) Raman spectra.

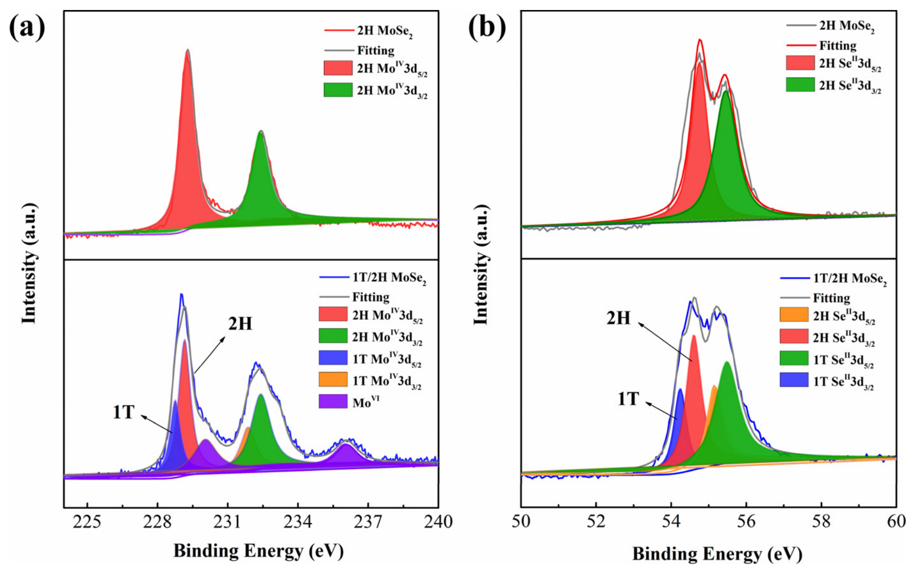

Fig. 3. XPS spectra of 1T/2H $MoSe_2$ and 2H $MoSe_2$.

2H $MoSe_2$ means better electronic conductivity and more facile electrode kinetics during HER [19].

3.2. Structure, morphology and optical property of heterostructure photocatalysts

The heterostructure photocatalysts i.e. 2H-MC or 1 T/2H-MC were obtained via a surface charge promoted self-assembly method driven by strong electrostatic attraction between the positively charged CdS and negatively charged $MoSe_2$ (Fig. S5). The XRD patterns of CdS, 2H-MC-10%, 1 T/2H-MC-10% all correspond to a hexagonal structure CdS (JCPDS card No. 02-0549), with no typical peaks of $MoSe_2$ detected, which may be ascribed to the relatively low content and weak diffraction intensity of $MoSe_2$ (Fig. S6) [18]. Fig. 5a shows the UV–vis spectra of CdS and all materials. It can be seen that bare CdS has a prominent absorption with an absorption edge at ~ 520 nm, corresponding to a band gap of ca. 2.38 eV by utilizing the Kubelka – Munk method, which is consistent with the reported value [37]. Interestingly, the same absorption edge as that of bare CdS was observed for the 2H-MC and 1 T/2H-MC samples, indicating that the band gap of CdS in 2H-MC and 1T/2H-MC is unchanged. Besides, the absorption intensities of all 1 T/2H-MC samples in visible light region from 520 to 800 nm enhance with the increase of 1T/2H $MoSe_2$ amount (1, 5, 10, 15 wt%), in accordance with the color change of samples from light yellow to greenish (insert pictures in Fig. 5a). Furthermore, compared with pure CdS and 2H-MC-10%, 1T/2H-MC-10% exhibits apparently enhanced intensity in absorbance at wavelengths above 520 nm (Fig. 5b), due to the better light absorption ability of 1 T/2H $MoSe_2$ cocatalyst itself (Fig. 4a). The BET surface areas of samples i.e. 2H-MC-10% and 1 T/2H-MC-10% were measured by N_2 adsorption desorption measurements (Fig. S7). Obviously, the BET surface area of 1T/2H-MC-10% is calculated to be ~ 23.69 m^2/g, which is higher than

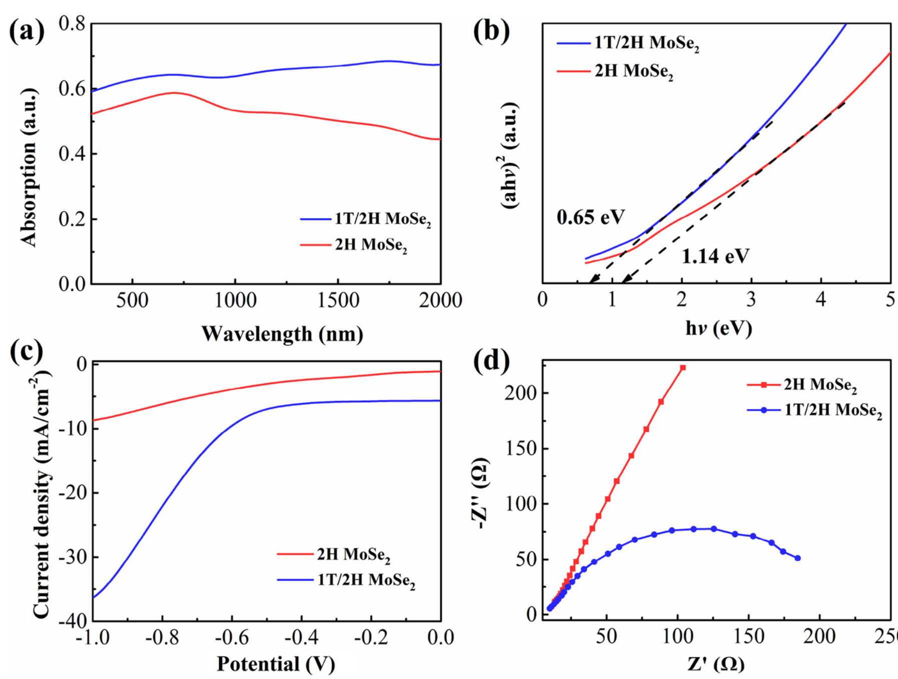

Fig. 4. Characterization of 1T/2H $MoSe_2$ and 2H $MoSe_2$: (a) UV–vis spectra, (b) bandgap energy (E_g), (c) I–V curves and (d) EIS Nyquist plots.

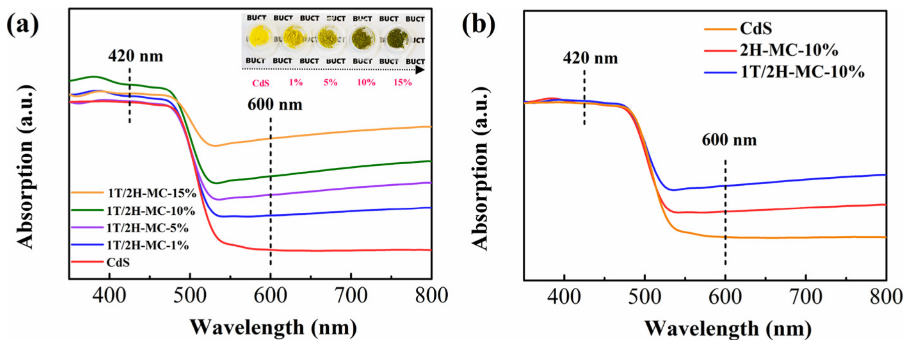

Fig. 5. (a) UV–vis absorption spectra of as-obtained 1T/2H-MC heterostructure photocatalysts containing different amounts of 1T/2H $MoSe_2$ (0, 1, 5, 10, 15 wt%). (b) UV–vis diffuse reflectance spectra of CdS, 2H-MC-10%, and 1 T/2H-MC-10%.

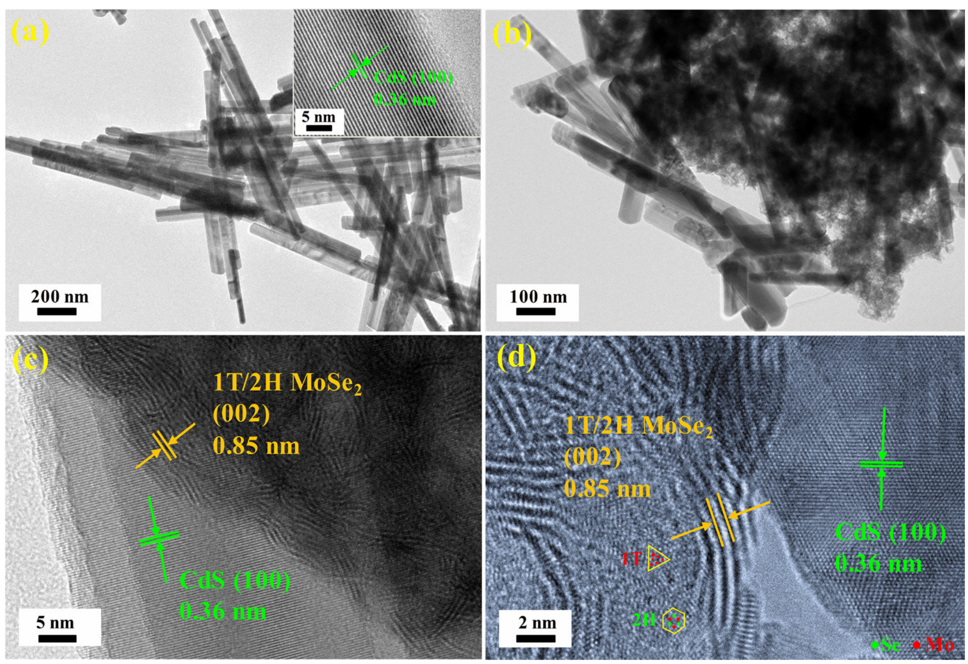

Fig. 6. (a) TEM image of pure CdS, insert: HRTEM image of pure CdS. (b) TEM, (c–d) HRTEM images of 1 T/2H-MC-10%.

that of 2H-MC-10% (~ 20.38 m^2/g). Such an increase in specific surface area of 1T/2H-MC-10% comparing with 2H-MC-10% may be beneficial for H_2 production because of more active edge sites to the reactants.

The morphologies of pure CdS and 1T/2H-MC-10% heterostructure were analyzed by TEM and HRTEM, as displayed in Fig. 6. Pure CdS exhibits 1D rod-shaped morphology (Fig. 6a), with an interlayer spacing of 0.36 nm that corresponds to the (100) plane of hexagonal CdS [19]. The TEM image in Fig. 6b shows the nanosheet-like 1T/2H $MoSe_2$ are decorated with rod-like CdS, confirming the successfully formation of 1T/2H-MC. The HRTEM images (Fig. 6c-d) of 1 T/2H-MC-10% demonstrate clear lattice fringes with the spacing of 0.36 and 0.85 nm, corresponding to the (001) plane of hexagonal CdS nanorods and the (002) plane of 1 T/2H $MoSe_2$ nanosheets, respectively. It is worth noting that 2H phase and 1T phase $MoSe_2$ are simultaneously observed in the 1 T/2H-MC-10% (Fig. 6d), further indicating the successful preparation of 1 T/2H-MC-10%. The EDS spectrum for 1T/2H-MC-10% (Fig. S8a) indicate the presence of Cd, S, Mo and Se elements and the weight ratio of 1 T/2H $MoSe_2$ in 1 T/2H-MC-10% is ~ 9.8 wt%. The EDS mappings (Fig. S8b-e) of 1 T/2H-MC-10% sample display the uniform distribution of Cd, S, Mo and Se, confirming 1 T/2H $MoSe_2$ are successfully loaded on the surface of CdS.

XPS assays were employed to study the chemical constitution and valence states of elements for CdS and 1 T/2H-MC-10% (Fig. 7a-f). As shown in Fig. 7a, the Cd, S, Mo, and Se elements are found in the XPS survey spectrum of 1T/2H-MC-10%. High-resolution XPS spectra (Fig. 7b-c) of Cd 3d in pure CdS show featured peaks of Cd $3d_{5/2}$ (404.7 eV) and Cd $3d_{3/2}$ (411.8 eV), together with S $2p_{3/2}$ (161.3 eV) and S $2p_{1/2}$ (162.3 eV) [37]. The binding energy of the Mo 3d in 1 T/2H-MC-10% appears at 232.1 eV (2H phase Mo $3d_{3/2}$) and the peak at 226.0 eV may be assigned to S 2 s (Fig. 7d) [38]. As for the Se 3d spectrum (Fig. 7e), four deconvoluted peaks at 53.3, 53.9, 54.2 and 54.8 eV are noticed in 1 T/2H-MC-10% sample. Notably, the binding energies of Cd 3d and S 2p in 1 T/2H-MC-10% are negatively shift by ca. 0.4 and 0.2 eV (Fig. 7b-c), respectively. Moreover, the binding energies of Mo 3d and Se 3d in 1 T/2H-MC-10% exhibit a positively shift by ca. 0.7 and 0.5 eV (Fig. 7d-e) compared with pure 1 T/2H $MoSe_2$ (Fig. 3a), respectively. These phenomena can be explained by partial electron transfers from CdS to 1 T/2H $MoSe_2$, i.e., increasing (decreasing) the electron density binding energies of Mo 3d and Se 3d (Cd 3d and S 2p), and further indicate the presence of strong electronic interaction between the interface of 1 T/2H $MoSe_2$ and CdS, promoting the photogenerated charge separation and transfer [39]. According to XPS analysis, 1 T/2H $MoSe_2$ in 1 T/2H-MC-10% heterostructure still contains ~ 32% 1 T phase. Fig. 7f shows the Raman spectra of CdS and 1 T/2H-MC-10% where characteristic peaks at 195, 235, 285, 350, 485 cm^{-1} corresponding to the 'J_1', 'A_{1g}', 'E^1_{2g}', 'J_2', 'J_3' bands of 1 T/2H $MoSe_2$ are observed for 1 T/2H-MC-10% sample, confirming the

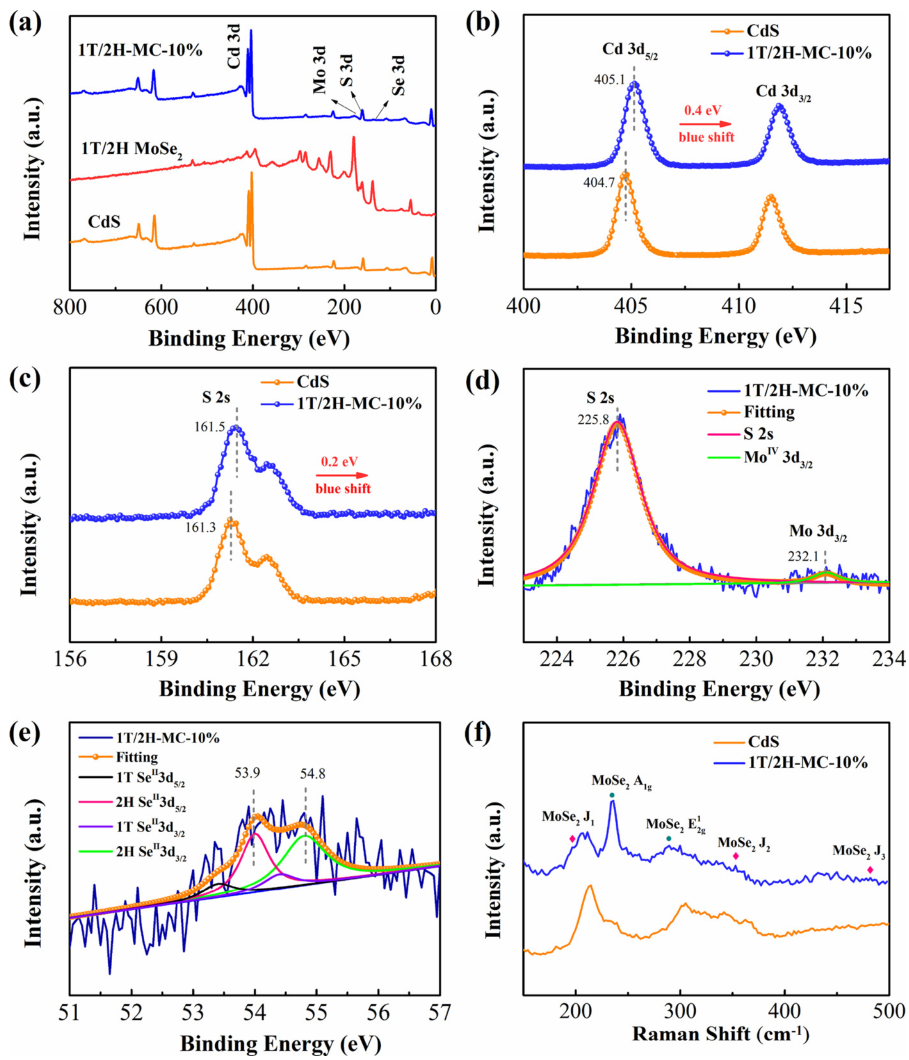

Fig. 7. (a) Survey XPS spectra of CdS, 1T/2H $MoSe_2$ and 1 T/2H-MC-10%. High-resolution XPS spectra of (b) Cd 3d and (c) S 2 s in CdS and 1 T/2H-MC-10%. (d) Mo 3d and (e) Se 3d spectra in 1 T/2H-MC-10%. (e) Raman spectra of CdS and 1 T/2H-MC -10%.

formation of a heterostructure with 1 T/2H $MoSe_2$ in the matrix of CdS [23]. Electron spin resonance (ESR) spectroscopy also confirm the phase of $MoSe_2$ existed in 1 T/2H-MC-10% heterostructure (Fig. S9).

3.3. Photocatalytic HER activities

The photocatalytic HER activity over all samples were performed under visible light irradiation. As shown in Fig. 8a, significant improvement in H_2 generation was established after coupling of 1 T/2H $MoSe_2$ to CdS, reaching a maximum of 93.4 mmol/g/h at 1 T/2H $MoSe_2$ loading of 10 wt%, being ~ 9 times higher than the rate observed for bare CdS (10.8 mmol/g/h). The surplus 1 T/2H $MoSe_2$ species reduce the reaction sites on CdS surface, thus leading to a decreased H_2 evolution activity of 1 T/2H-MC-15% [18]. The H_2 evolution rate of 2H-MC-10% under visible-light (λ > 470 nm) irradiation (Fig. S10) is also tremendously increased to 55.2 mmol/g/h, which is ~ 22 times higher than that of CdS (2.5 mmol/g/h). Furthermore, we have also performed the measurements on the photocatalytic performance of 1 T/2H-MC-10% photocatalysts with different dosages (Fig. S11a). Apparently, as the photocatalyst dosages continuously increased, the total amount of H_2 evolution increased. Besides, cycle stability assay of 1 T/2H-MC-10% (6 mg) demonstrated that 1 T/2H-MC can be applied as a stable photocatalyst for H_2 evolution (Fig. S11b). The corresponding AQY of 1 T/2H-MC-10% (33.2% at 420 nm and 1.9% at 600 nm), which are both higher than that of CdS (0.8% at 420 nm and 0% at 600 nm). Meanwhile, the dependence of the quantum yield of the photocatalytic H_2 evolution of CdS and 1 T/2H-MC-10% on the irradiation wavelengths was also offered (Fig. S12). As can be seen in Fig. 8b, the photocatalytic HER performance of 2H-MC show a substantially lower H_2 evolution rate in comparison with those of 1 T/2H-MC photocatalysts. It is reasonable because 1 T/2H $MoSe_2$ shows more active edge sites and better electrical conductivity as compared to 2H $MoSe_2$. Notably, as shown in Fig. 8c-d, the observed photocatalytic HER rate of 1 T/2H-MC-10% (93.4 mmol/g/h) is much higher than that of Pt/CdS (50.4 mmol/g/h). This result highlights that 1 T/2H $MoSe_2$ possibly becomes an alternative cocatalyst for the replacement of expensive and scarce Pt due to its higher efficiency and much lower cost [40]. Stability is a decisive factor when considering the practical application of photocatalyst. The cycling test over the optimal 1 T/2H-MC-10% shows negligible photoactivity loss after 8 consecutive cycles under visible light (λ > 420 nm) irradiation (Fig. 8e). Additionally, we carried out photocatalytic HER catalyzed by 1 T/2H-MC-10% under a prolonged visible light irradiation (λ > 420 nm) of 35 h (Fig. 8f). No obvious decay of photocatalytic HER was observed, suggesting its durability and potential of practical application. Furthermore, the structure and morphology characterization of 1 T/2H-MC-10% after photocatalytic reaction was carried out, including XRD, XPS, TEM, and HRTEM analyses. Based on the results shown in Fig. S13-15, 1 T/2H-$MoSe_2$ and

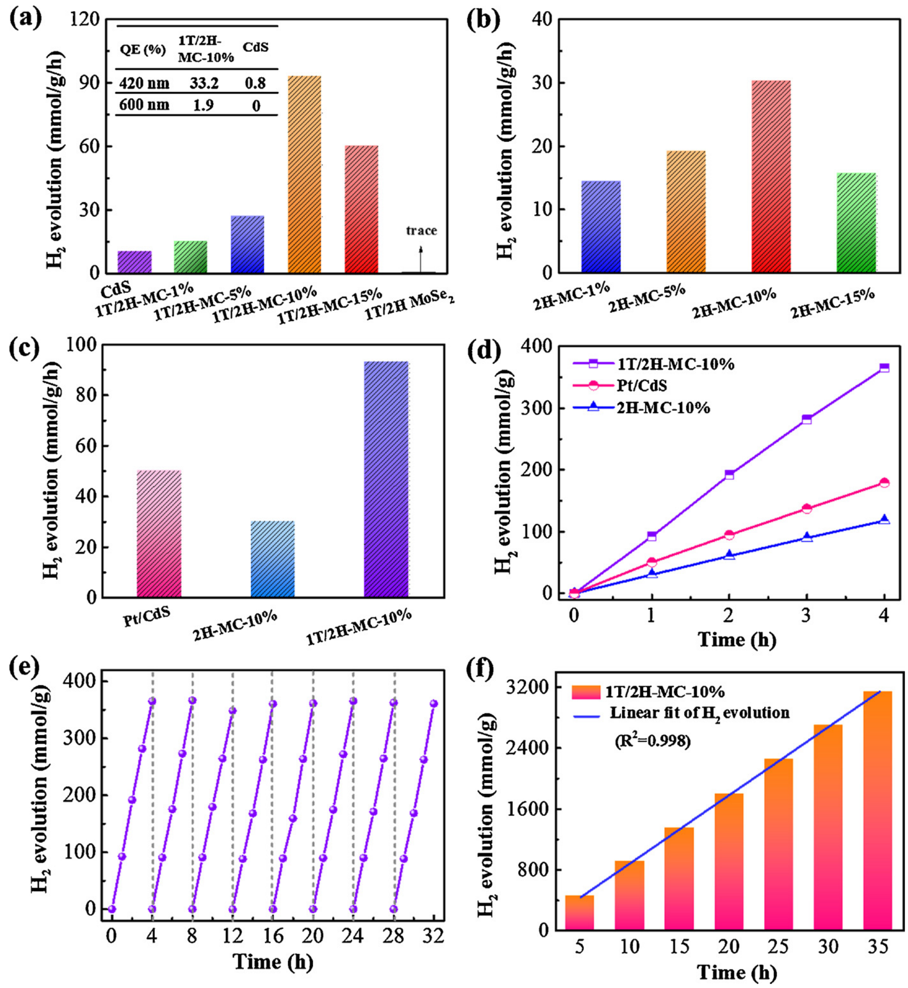

Fig. 8. (a–b) H_2 yield rates of different samples under visible light irradiation ($\lambda > 420$ nm). (c–d) Comparison of photocatalytic H_2 evolution activities over 1 T/2H-MC-10%, 2H-MC-10%, Pt/CdS. (e) Recyclability of hydrogen evolution tests and (f) Photocatalytic H_2 evolution under a prolonged visible light irradiation ($\lambda > 420$ nm) of 35 h catalyzed by 1 T/2H-MC-10%.

1 T/2H-MC are highly stable under visible light irradiation.

3.4. Origin and analysis of the enhanced performance

To explore reasons for this significant enhancement of the photocatalytic HER over 1 T/2H-MC heterostructure, a series of complementary photo- and electrochemical (PEC) characterizations were carried out. PEC analyses are considered as a powerful tool to characterize photogenerated charge carrier migration and separation efficiency of samples. Fig. 9a shows the time-dependent photo-current responses of various photocatalysts with 20 s simulated visible light on/off ; cycles. Not surprisingly, 1 T/2H-MC-10% exhibits the highest photocurrent intensity, suggesting efficiently excited charge carriers separation between 1 T/2H $MoSe_2$ and CdS [19]. Furthermore, the 1 T/2H-MC-10% sample shows a relatively stronger photoresponse compared to pure CdS and 2H-MC-10% as ascertained by the I–V curves (Fig. 9b). To further confirm the enhanced charge separation efficiency, the EIS Nyquist plots of pure CdS, 2H-MC-10% and 1 T/2H-MC-10% electrodes were measured (Fig. 9c) and could be fitted to an equivalent circuit (the inset). As summarized in Table S2, the value of R_{ct} for 1 T/2H-MC-10% is dramatically lower than those of bare CdS and 2H-MC-10%, further inferring the prevailing roles of loaded 1 T/2H $MoSe_2$ as the H_2 evolution cocatalysts which accelerate the charge transport and separation of CdS [41,42]. Such results elucidate that the heterostructure presents a lower charge transfer resistance and boosted electrical conductivity, thus facilitating eff ;ective interfacial electron transfer at the interface between 1 T/2H $MoSe_2$ and CdS.

To further evaluate the separation efficiency and charge carrier transport of samples, PL technologies were carried out, including SS-PL and TR-PL. As shown in Fig. 9d, the broad fluorescence peaks of all samples appearing at ~ 520 nm can be assigned to near-band-edge emission of CdS [43]. Pure CdS shows the strongest emission due to high recombination of photoexcited charges. Meanwhile, PL intensity of 1 T/2H-MC-10% is much lower than that of CdS and 2H-MC-10%, indicating that 1 T/2H $MoSe_2$ favors the accelerated charge carrier transfer, thereby enhancing the electron–hole pair separation and further facilitating the photocatalytic HER [44,45]. In addition, Fig. 9e displays the TR-PL spectra of CdS and 1 T/2H-MC-10%, which probe the specific charge carrier dynamics of nanosystems [41,46]. The PL lift-times of CdS and 1 T/2H-MC-10% are calculated by fitting biexponential kinetics function with the following exponential fitting Eq. (2):

$$Fit = A + B_1 exp\left\{-\frac{t}{\tau_1}\right\} + B_2 exp\left\{-\frac{t}{\tau_2}\right\} \tag{2}$$

where A, B_1, B_2, are constants and obtained after fitting every decay curve. Simultaneously, τ_1 is originated from the nonradiative recombination of charge carriers in the defect states of CdS, whereas the longer lifetime component of τ_2 is caused by the recombination of free excitons in the CdS [23]. For 1T/2H-MC-10%, the emission lifetimes of both components (τ_1 = 1.73 ns, τ_2 = 7.56 ns) are shorter than that of the corresponding CdS counterpart (τ_1 = 1.87 ns, τ_2 = 8.57 ns). Then, on the basis of the fitting data, the average life-time (τ_{avg}) is calculated

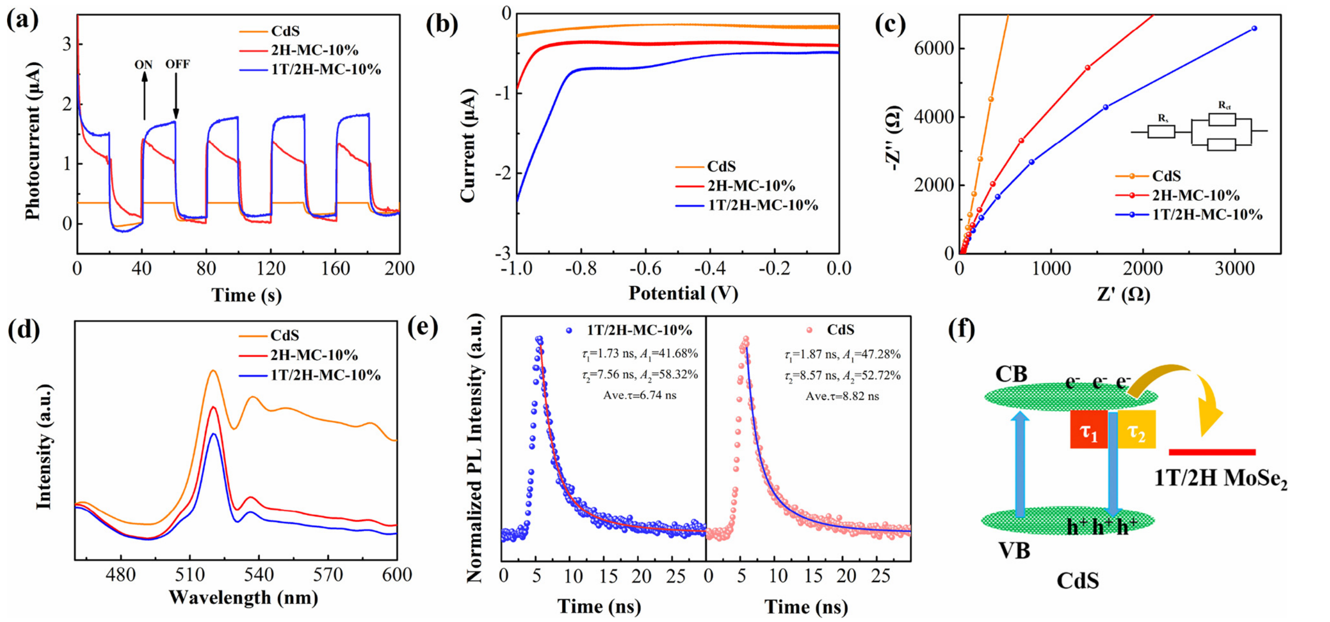

Fig. 9. (a) Transient photocurrent responses, (b) I–V curves, (c) EIS spectra and SS-PL spectra of CdS, 2H-MC-10% and 1 T/2H-MC-10%. (e) TR-PL decay of CdS, 1 T/2H-MC-10%. (f) Schematic illustration of the interfacial charge carrier transfer in 1 T/2H-MC-10%.

by following Eq. (3):

$$\tau_{avg} = \frac{B_1\tau_1^2 + B_2\tau_2^2}{B_1\tau_1 + B_2\tau_2} \tag{3}$$

τ_{avg}, which reflects the overall emission decay behavior of sample, has also displayed an obvious decrease for 1 T/2H-MC-10% (6.74 ns) as compared with that of CdS (8.52 ns). The corresponding observations of PL quenching and lifetime reduction suggest the establishment of an electron transfer channel from CdS to 1 T/2H $MoSe_2$ in a nonradiative quenching pathway (Fig. 9e).

Additionally, we estimated the conduction band (CB) and flat band potentials of the CdS, 2H $MoSe_2$ and 1 T/2H $MoSe_2$ via Mott–Schottky experiments (Fig. 10a-c) [47]. The flat band potentials obtained by Mott–Schottky analysis are approximately equal to -1.07 V, -0.81 and -0.74 V vs. Ag/AgCl for CdS, 2H $MoSe_2$ and 1 T/2H $MoSe_2$, respectively. However, it is well known that the CB potential of n-type semiconductors is more negative (by ~ 0.10 V) than the flat band potential, allowing us to estimate CB potentials as approximately -0.77, -0.51 and -0.44 V vs. NHE ($E_{NHE} = E_{Ag/AgCl} + 0.197$) for CdS, 2H $MoSe_2$ and 1 T/2H $MoSe_2$, respectively [48,49]. Base on the above data and analysises, the band structure of the photocatalysts can be depicted in Fig. 10d. According to the H_2 evolution “band matching” theory [50], the photo-excited electrons from CdS would be easier to be injected into the CB of 1 T/2H $MoSe_2$ because of lower and favorable energy level of 1 T/2H

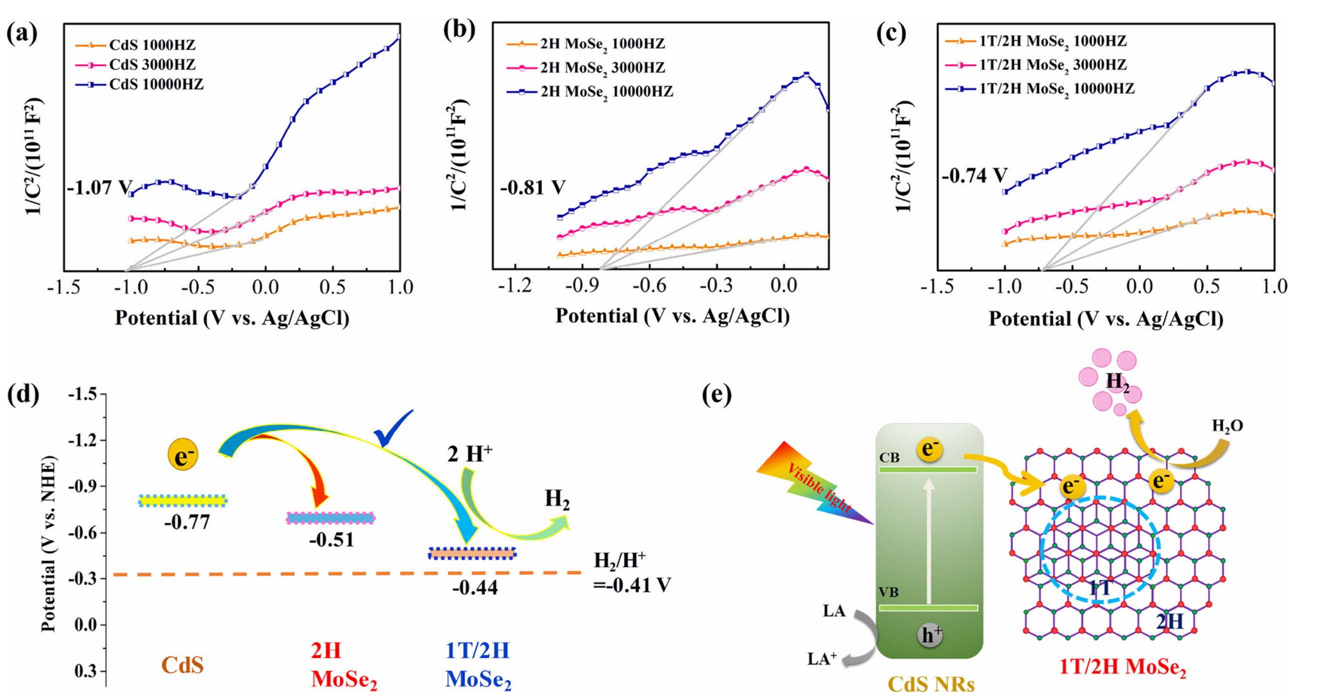

Fig. 10. (a–c) Mott-Schottky plots of CdS, 2H $MoSe_2$ and 1 T/2H $MoSe_2$. (d) Schematic illustration of the band structure of CdS, 2H $MoSe_2$ and 1 T/2H $MoSe_2$. (e) Schematic illustration of the photogenerated charge transfer in the 1 T/2H-MC heterostructure under visible light irradiation (λ > 420 nm).

$MoSe_2$. This sketch could help decipher the reasons why 1 T/2H $MoSe_2$ exhibits such higher activity as a cocatalyst for photocatalytic HER under visible irradiation than 2H $MoSe_2$. As discussed above, a plausible mechanism for high H_2 evolution performance of the 1 T/2H-MC heterostructure was proposed and illustrated in Fig. 10e. Upon visible-light irradiation, photogenerated electron–hole pairs were generated in CdS. The photoexcited electrons quickly transfer from CdS to 1 T/2H $MoSe_2$ cocatalyst due to the electronic interaction and the matched band potentials. Meanwhile, the photogenerated holes in the valence band of CdS can be consumed by the sacrificial reagents (lactic acid). Consequently, the photogenerated electrons and holes can be eff ;ectively separated, and the photocatalytic H_2 evolution activity gets promoted for the 1 T/2H-MC heterostructure.

4. Conclusions

In summary, a novel stable multiphasic 1 T/2H $MoSe_2$ nanosheets cocatalyst has been successfully synthesized via a facile hydrothermal method and subsequently integrated with 1D CdS nanorods for photocatalytic HER under visible light irradiation. For comparison, conventional 2H $MoSe_2$ and corresponding heterostructure 2H-MC were synthesized in parallel. The optimized 1 T/2H-MC-10% exhibits remarkably enhanced visible-light (λ > 420 nm) photocatalytic H_2 production rate of 93.4 mmol/g/h, much higher than those of pure CdS, 2H-MC and commonly-used Pt/CdS. Such an H_2 production rate also exceeds all reported $MoSe_2$-based photocatalysts. This increased HER performance can be attributed to the following aspects of reasons: 1) 1 T/2H $MoSe_2$ exhibits high structural stability, good electrical conductivity, abundant active sites beneficial to H_2 evolution; 2) the electronic interaction as well as favorable band position between the 1 T/2H $MoSe_2$ and CdS can eff ;ectively enhance transfer ability of charge and thus retard the recombination of electron-hole pairs. This work demonstrates a potential replacement of 1 T/2H $MoSe_2$ for noble-metal Pt as cocatalyst for high-efficiency photocatalytic HER and provide an opportunity to develop other 1 T/2H $MoSe_2$-based heterostructure photocatalysts in energy-generation field.

Acknowledgement

The work was supported by the National Natural Science Foundation of China (Nos. 21377011, 21476019, 21676017).

Appendix A. Supplementary data

Supplementary material related to this article can be found, in the online version, at doi:https://doi.org/10.1016/j.apcatb.2018.07.002.

References

[1] K. Maeda, K. Domen, Photocatalytic water splitting: recent progress and future challenges, J. Phys. Chem. Lett. 1 (2010) 2655–2661.
[2] L. Yuan, C. Han, M.Q. Yang, Y.J. Xu, Photocatalytic water splitting for solar hydrogen generation: fundamentals and recent advancements, Int. Rev. Phys. Chem. 35 (2016) 1–36.
[3] G. Zhao, Y. Sun, W. Zhou, X. Wang, K. Chang, G. Liu, H. Liu, T. Kako, J. Ye, Superior photocatalytic H_2 production with cocatalytic Co/Ni species anchored on sulfide semiconductor, Adv. Mater. 29 (2017) 1703258.
[4] X. Wang, K. Maeda, X. Chen, K. Takanabe, K. Domen, Y. Hou, X. Fu, M. Antonietti, Polymer semiconductors for artificial photosynthesis: hydrogen evolution by mesoporous graphitic carbon nitride with visible light, J. Am. Chem. Soc. 131 (2009) 1680–1681.
[5] D.J. Martin, P.J. Reardon, S.J. Moniz, J. Tang, Visible light-driven pure water splitting by a nature-inspired organic semiconductor-based system, J. Am. Chem. Soc. 136 (2014) 12568–12571.
[6] Q. Liang, Z. Li, X. Yu, Z.H. Huang, F. Kang, Q.H. Yang, Macroscopic 3D porous graphitic carbon nitride monolith for enhanced photocatalytic hydrogen evolution, Adv. Mater. 27 (2015) 4634–4639.
[7] L. Lu, M. Lv, D. Wang, G. Liu, X. Xu, Efficient photocatalytic hydrogen production over solid solutions $Sr_{1-x}Bi_xTi_{1-x}Fe_xO_3$ ($0 \le x \le 0.5$), Appl. Catal. B:Environ. 200 (2017) 412–419.
[8] P.D. Tran, L. Xi, S.K. Batabyal, L.H. Wong, J. Barber, J.S. Loo, Enhancing the photocatalytic efficiency of TiO_2 nanopowders for H_2 production by using non-noble transition metal co-catalysts, Phys. Chem. Chem. Phys. 14 (2012) 11596–11599.
[9] A.K. Agegnehu, C.J. Pan, J. Rick, J.F. Lee, W.N. Su, B.J. Hwang, Enhanced hydrogen generation by cocatalytic Ni and NiO nanoparticles loaded on graphene oxide sheets, J. Mater. Chem. 22 (2012) 13849–13854.
[10] W. Zhang, Y. Wang, Z. Wang, Z. Zhong, R. Xu, Highly efficient and noble metal-free NiS/CdS photocatalysts for H_2 evolution from lactic acid sacrificial solution under visible light, Chem. Commun. 46 (2010) 7631–7633.
[11] K. Chang, Z. Mei, T. Wang, Q. Kang, S. Ouyang, J. Ye, MoS_2/graphene cocatalyst for efficient photocatalytic H_2 evolution under visible light irradiation, ACS Nano 8 (2014) 7078–7087.
[12] K. Chang, X. Hai, H. Pang, H. Zhang, L. Shi, G. Liu, H. Liu, G. Zhao, M. Li, J. Ye, Targeted synthesis of 2H- and 1T-phase MoS_2 monolayers for catalytic hydrogen evolution, Adv. Mater. 28 (2016) 10033–10041.
[13] A. Ambrosi, Z. Sofer, M. Pumera, 2H→1T phase transition and hydrogen evolution activity of MoS_2, $MoSe_2$, WS_2 and WSe_2 strongly depends on the MX_2 composition, Chem. Commun. 51 (2015) 8450–8453.
[14] J. Kibsgaard, Z. Chen, B.N. Reinecke, T.F. Jaramillo, Engineering the surface structure of MoS_2 to preferentially expose active edge sites for electrocatalysis, Nat. Mater. 11 (2012) 963–969.
[15] J. Xie, H. Zhang, S. Li, R. Wang, X. Sun, M. Zhou, J. Zhou, X.W. Lou, Y. Xie, Defect-rich MoS_2 ultrathin nanosheets with additional active edge sites for enhanced electrocatalytic hydrogen evolution, Adv. Mater. 25 (2013) 5807–5813.
[16] D. Damien, A. Anil, D. Chatterjee, M.M. Shaijumon, Direct deposition of $MoSe_2$ nanocrystals onto conducting substrates: towards ultra-efficient electrocatalysts for hydrogen evolution, J. Mater. Chem. A 5 (2017) 13364–13372.
[17] C. Dai, Z. Zhou, C. Tian, Y. Li, C. Yang, X. Gao, X. Tian, Large scale synthesis of graphene-like $MoSe_2$ nanosheets for efficient hydrogen evolution reaction, J. Phys. Chem. C 121 (2017) 1974–1981.
[18] S. Hong, D.P. Kumar, E.H. Kim, H. Park, M. Gopannagari, D.A. Reddy, T.K. Kim, Earth abundant transition metal-doped few-layered MoS_2 nanosheets on CdS nanorods for ultra-efficient photocatalytic hydrogen production, J. Mater. Chem. A 5 (2017) 20851–20859.
[19] X.H. Zhang, N. Li, J. Wu, Y.Z. Zheng, X. Tao, Defect-rich O-incorporated 1T-MoS_2 nanosheets for remarkably enhanced visible-light photocatalytic H_2 evolution over CdS: the impact of enriched defects, Appl. Catal. B: Environ. 229 (2018) 227–236.
[20] B. Zheng, Y. Chen, F. Qi, X. Wang, W. Zhang, Y. Li, X. Li, 3D-hierarchical $MoSe_2$ nanoarchitecture as a highly efficient electrocatalyst for hydrogen evolution, 2d Mater. 4 (2017) 025092.
[21] S. Larentis, B. Fallahazad, E. Tutuc, Field-effect transistors and intrinsic mobility in ultra-thin $MoSe_2$, Appl. Phys. Lett. 101 (2012) 223104.
[22] S. Kou, X. Guo, X. Xu, J. Yang, TiO_2 on $MoSe_2$ nanosheets as an advanced photocatalyst for hydrogen evolution in visible light, Catal. Commun. 106 (2018) 60–63.
[23] M.Q. Yang, Y.J. Xu, W. Lu, K. Zeng, H. Zhu, Q.H. Xu, G.W. Ho, Self-surface charge exfoliation and electrostatically coordinated 2D hetero-layered hybrids, Nat. Commun. 8 (2017) 14224.
[24] D. Zeng, P. Wu, W.J. Ong, B. Tang, M. Wu, H. Zheng, Y. Chen, D.L. Peng, Construction of network-like and flower-like 2H-$MoSe_2$ nanostructures coupled with porous g-C_3N_4 for noble-metal-free photocatalytic H_2 evolution under visible light, Appl. Catal. B: Environ. 233 (2018) 26–34.
[25] S. Deng, Y. Zhong, Y. Zeng, Y. Wang, Z. Yao, F. Yang, S. Lin, X. Wang, X. Lu, X. Xia, Directional construction of vertical nitrogen-doped 1T-2H $MoSe_2$/graphene shell/core nanoflake arrays for efficient hydrogen evolution reaction, Adv. Mater. 29 (2017) 1700748.
[26] T. Xiang, S. Tao, W. Xu, Q. Fang, C. Wu, D. Liu, Y. Zhou, A. Khalil, Z. Muhammad, W. Chu, Stable 1T-$MoSe_2$ and carbon nanotubes hybridized flexible film: binder-free and high-performance Li-Ion anode, ACS Nano 11 (2017) 6483–6491.
[27] Y. Ying, Y. Zhang, T. Gao, Y. Tai, X. Zhang, J. Han, X. Wang, Z. Zhang, X. Ping, Z. Peng, Synergistic phase and disorder engineering in 1T-$MoSe_2$ nanosheets for enhanced hydrogen-evolution reaction, Adv. Mater. 29 (2017) 1700311.
[28] J. Zhang, T. Wang, P. Liu, Y. Liu, J. Ma, D. Gao, Enhanced catalytic activities of metal-phase-assisted 1T@2H-$MoSe_2$ nanosheets for hydrogen evolution, Electrochim. Acta 217 (2016) 181–186.
[29] X. Hu, W. Zhang, X. Liu, Y. Mei, Y. Huang, Nanostructured Mo-based electrode materials for electrochemical energy storage, Chem. Soc. Rev. 46 (2015) 2376–2404.
[30] Z. Sun, H. Zheng, J. Li, P. Du, Extraordinarily efficient photocatalytic hydrogen evolution in water using semiconductor nanorods integrated with crystalline Ni_2P cocatalyst, Energy Environ. Sci. 8 (2015) 2668–2676.
[31] Y. Qu, H. Medina, S.W. Wang, Y.C. Wang, C.W. Chen, T.Y. Su, A. Manikandan, K. Wang, Y.C. Shih, J.W. Chang, Wafer scale phase-engineered 1T- and 2H-$MoSe_2$ /Mo core-shell 3D-hierarchical nanostructures toward efficient electrocatalytic hydrogen evolution reaction, Adv. Mater. 28 (2016) 9831–9838.
[32] S. Mao, Z. Wen, S. Ci, X. Guo, K.K. Ostrikov, J. Chen, Hydrogen evolution: perpendicularly oriented $MoSe_2$/graphene nanosheets as advanced electrocatalysts for hydrogen evolution, Small 11 (2015) 414–419.
[33] M.A. Lukowski, A.S. Daniel, C.R. English, F. Meng, A. Forticaux, R.J. Hamers, S. Jin, Highly active hydrogen evolution catalysis from metallic WS_2 nanosheets, Energy Environ. Sci. 7 (2014) 2608–2613.
[34] P. Liu, Y. Liu, W. Ye, J. Ma, D. Gao, Flower-like N-doped MoS_2 for photocatalytic degradation of RhB by visible light irradiation, Nanotechnology 27 (2016) 225403.
[35] D. Wang, X. Zhang, S. Bao, Z. Zhang, F. Hao, Z. Wu, Phase-engineering of multiphasic 1T/2H MoS_2 catalyst for highly efficient hydrogen evolution, J. Mater. Chem. A 5 (2016) 2681–2688.
[36] Y. Sun, X. Hu, W. Luo, Y. Huang, Self-assembled hierarchical MoO_2/graphene

nanoarchitectures and their application as a high-performance anode material for lithium-ion batteries, ACS Nano 5 (2011) 7100–7107.
[37] D.A. Reddy, H. Park, R. Ma, D.P. Kumar, M. Lim, T.K. Kim, Heterostructured WS_2-MoS_2 ultrathin nanosheets integrated on CdS nanorods to promote charge separation and migration and improve solar-driven photocatalytic hydrogen evolution, ChemSusChem 10 (2017) 1563–1570.
[38] J. Chen, X.J. Wu, L. Yin, B. Li, X. Hong, Z. Fan, B. Chen, C. Xue, H. Zhang, One-pot synthesis of CdS nanocrystals hybridized with single-layer transition-metal dichalcogenide nanosheets for efficient photocatalytic hydrogen evolution, Angew. Chem. Int. Ed. 54 (2015) 1210–1214.
[39] S. Zhang, H. Yang, H. Gao, R. Cao, J. Huang, X. Xu, One-pot synthesis of CdS irregular nanospheres hybridized with oxygen-incorporated defect-rich MoS_2 ultrathin nanosheets for efficient photocatalytic hydrogen evolution, ACS Appl. Mater. Interfaces 9 (2017) 23635–23646.
[40] H. Tang, K. Dou, C.C. Kaun, Q. Kuang, S. Yang, $MoSe_2$ nanosheets and their graphene hybrids: synthesis, characterization and hydrogen evolution reaction studies, J. Mater. Chem. A 2 (2013) 360–364.
[41] N. Zhang, M.Q. Yang, Z.R. Tang, Y.J. Xu, Toward improving the graphene-semiconductor composite photoactivity via the addition of metal ions as generic interfacial mediator, ACS Nano 8 (2014) 623–633.
[42] C. Han, Z. Chen, N. Zhang, J.C. Colmenares, Y.J. Xu, Hierarchical hybrids: hierarchically CdS decorated 1D ZnO nanorods-2D graphene hybrids: Low temperature synthesis and enhanced photocatalytic performance, Adv. Funct. Mater. 25 (2015) 170-170.
[43] S. Liu, N. Zhang, Z.R. Tang, Y.J. Xu, Synthesis of one-dimensional CdS@TiO_2 core-shell nanocomposites photocatalyst for selective redox: the dual role of TiO_2 shell, ACS Appl. Mater. Interfaces 4 (2012) 6378–6385.
[44] X.L. Yin, L.L. Li, W.J. Jiang, Z. Yun, Z. Xiang, L.J. Wan, J.S. Hu, MoS_2/CdS nanosheets-on-nanorod heterostructure for highly efficient photocatalytic H_2 generation under visible light irradiation, ACS Appl. Mater. Interfaces 8 (2016) 15258–15266.
[45] H.B. Fang, X.H. Zhang, J. Wu, N. Li, Y.Z. Zheng, X. Tao, Fragmented phosphorus-doped graphitic carbon nitride nanoflakes with broad sub-bandgap absorption for highly efficient visible-light photocatalytic hydrogen evolution, Appl. Catal. B: Environ. 225 (2017) 397–405.
[46] Z. Zhang, Y. Huang, K. Liu, L. Guo, Q. Yuan, B. Dong, Multichannel-improved charge-carrier dynamics in well-designed hetero-nanostructural plasmonic photocatalysts toward highly efficient solar-to-fuels conversion, Adv. Mater. 27 (2015) 5906–5914.
[47] J. Wu, N. Li, X.H. Zhang, H.B. Fang, Y.Z. Zheng, X. Tao, Heteroatoms binary-doped hierarchical porous g-C_3N_4 nanobelts for remarkably enhanced visible-light-driven hydrogen evolution, Appl. Catal. B: Environ. 226 (2018) 61–70.
[48] Y.J. Yuan, H.W. Lu, Z.T. Yu, Z.G. Zou, Noble-metal-free molybdenum disulfide cocatalyst for photocatalytic hydrogen production, ChemSusChem 8 (2015) 4113–4127.
[49] S. Saha, G. Das, J. Thote, R. Banerjee, Photocatalytic metal-organic framework from CdS quantum dot incubated luminescent metallohydrogel, J. Am. Chem. Soc. 136 (2014) 14845–14851.
[50] L. Wang, X. Liu, J. Luo, X. Duan, J. Crittenden, C. Liu, S. Zhang, Y. Pei, Y. Zeng, X. Duan, Active site self-optimization by irreversible phase transition of 1T-MoS_2 in photocatalytic hydrogen evolution, Angew. Chem. Int. Ed. 56 (2017) 7610–7614.